Plane wave method for elastic wave scattering by a heterogeneous fracture

Seiji Nakagawa [a], Kurt T. Nihei, and Larry R. Myer

Earth Sciences Division, Lawrence Berkeley National Laboratory, Berkeley, California

Received:

Running title: plane wave method for a heterogeneous fracture

Abbreviated title: plane wave method for a heterogeneous fracture

[a]Electronic-mail: snakagawa@lbl.gov

ABSTRACT

A plane-wave method for computing the three-dimensional scattering of propagating elastic waves by a planar facture with heterogeneous fracture compliance distribution is presented. This method is based upon the spatial Fourier transform of the seismic displacement-discontinuity (SDD) boundary conditions (also called linear slip interface conditions), and therefore, called the wavenumber-domain SDD method (wd-SDD method). The resulting boundary conditions explicitly show the coupling between plane waves with an incident wavenumber component (specular component) and scattered waves that do not follow the Snell's law (non-specular components) if the fracture is viewed as a planar boundary. For a spatially periodic fracture compliance distribution, these boundary conditions can be cast into a linear system of equations that can be solved for the amplitudes of individual wave modes and wavenumbers. We demonstrate the developed technique for a simulated fracture with a stochastic (correlated) surface compliance distribution. Low and high-frequency solutions of the method are also compared to the predictions by low-order Born series in the weak and strong scattering limit.

PACS numbers: 43.20.Gp, 43.20.Px, 43.58.Ta

I. INTRODUCTION

At micro scales, fractures in rocks, metals and ceramics can take many different forms including aligned open cracks, two surfaces in imperfect contact and a planar, thin zone filled with materials more compliant than the background medium (e.g., Liu et al, 2000). Since a fracture scatters propagating elastic waves as a function of the fracture geometry and mechanical properties, they can be detected and characterized from the scattering behavior of the waves.

The micro-scale geometry and spatial property variations of a fracture, however, cannot be resolved using elastic waves if these heterogeneous features are much smaller than the wavelengths. Instead, these heterogeneities are likely to affect the scattering behavior of the waves through static, effective mechanical properties of the fracture that are determined at some sub-wavelength scale larger than the heterogeneities themselves. This is one of the basic principles of the seismic displacement-discontinuity (SDD) boundary conditions (also known as linear slip interface conditions) commonly used for examining elastic wave scattering by fractures. The SDD conditions assume a linear relationship between the wave-introduced, small relative displacement and stress across a fracture, via material parameters called fracture stiffness and its inverse, fracture compliance (Schoenberg, 1980). Baik and Thompson (1983) showed that the fracture compliance can be determined analytically for fractures consisting of sparsely distributed, co-planar circular cracks and of contact patches between half spaces. Angel and Achenbach (1985) showed that elastic wave scattering off a fracture, consisting of aligned microcracks, can be modeled by the SDD conditions for long wavelengths. From laboratory ultrasonic transmission tests across a synthetic fracture with known, regular geometry, Myer et al. (1985) found good agreement between measured waves and theoretical prediction by the SDD model.

Theoretical studies based upon the SDD model on the elastic wave scattering by fractures are limited to, or assume, fractures with a homogeneous distribution of fracture compliance on the fracture plane (Schoenberg, 1980; Pyrak-Nolte and Cook, 1987; Rokhlin and Wang, 1991; Nakagawa et al., 2002). This is because the conventional SDD model, when used with plane wave theory, requires a “range-independent” (material properties do not vary along the fracture plane) fracture compliance distribution. Naturally occurring fractures are, however,

heterogeneous, with the micro scale properties varying along the fracture plane. This gives rise to fracture compliance that is spatially heterogeneous and, possibly, correlated. Since the heterogeneity of a fracture has a great impact on the hydraulic and mechanical properties of the fracture (Pyrak-Nolte et al., 1987; Buck et al., 1987; Jones and Knipe, 1996; Hakami and Larsson, 1996), understanding the effect of the heterogeneity on the scattering of elastic waves can provide valuable tools for geophysical and nondestructive characterization of the fracture properties.

In this article, we present analytical and numerical techniques to examine the elastic wave scattering by a heterogeneous fracture, based on the "local" SDD boundary conditions and the plane wave theory. This is achieved by applying a spatial Fourier transform to the SDD conditions with "local" fracture compliance that is a function in space. For this reason, this method is called the wavenumber domain seismic displacement discontinuity method (wd-SDD method). Previously, the local SDD model was used in geometric ray approximations. Pyrak-Nolte and Nolte (1992) examined the apparent, scattering induced frequency dependence of fracture compliance assuming that the compliance varied much more slowly compared to the wavelength (high-frequency ray approximation). Nihei (1989) and Oliger et al. (2003) used Kirchhoff approximations to take into account the diffraction of waves transmitted across a heterogeneous fracture. In the Kirchhoff approximations, the amplitudes and phases of the transmitted waves across a fracture are computed at each location on the fracture, assuming that the fracture is planar and has a single value of fracture compliance assigned to that location. In contrast, the wd-SDD method is not limited to high frequencies and takes into account the interactions between different locations on the fracture. Although numerical methods such as the boundary element method (Mikata and Achenbach, 1988) and the finite difference method (Punjanni and Bond, 1986; Coates and Schoenberg, 1995) can also be used to examine the scattering of elastic waves at full range of frequencies, applications of these methods to three-dimensional problems results in high computational costs, particularly large computer memory. Further, the analytical nature of the introduced method can provide clearer insights into the mechanism of wave scattering by a heterogeneous fracture.

II. THEORY

A. Plane wave analysis

We first hypothesize that the "local fracture compliance" can be defined for a fracture. This means that the dynamic behavior of a real fracture is well approximated by the behavior of an interface between half-spaces with a heterogeneous distribution of compliance which is measured locally at some length scale much smaller than the seismic (elastic wave) wavelengths. This approach is commonly taken to numerically simulate wave scattering by fractures with heterogeneous surface contacts using the boundary element method and the finite difference method.

In our model, we also assume that the dimension of a fracture in the fracture-normal direction, such as the surface roughness and waviness, is much smaller than considered seismic wavelengths, and therefore, the fracture can be treated as a plane. For the local fracture compliance model, the SDD boundary conditions are specified at each spatial location on the fracture on the *x*, *y* plane as (Figure 1)

$$\boldsymbol{\sigma}^{+}(x,y) = \boldsymbol{\sigma}^{-}(x,y) \equiv \boldsymbol{\sigma}(x,y), \quad (1)$$

$$\boldsymbol{\eta}(x,y)\boldsymbol{\sigma}(x,y) = [\mathbf{u}](x,y), \quad (2)$$

where the displacement-discontinuity vector $[\mathbf{u}]$, stress vectors $\boldsymbol{\sigma}^{\pm}$, $\boldsymbol{\sigma}$, and the compliance matrix $\boldsymbol{\eta}$ are defined as

$$[\mathbf{u}](x,y) \equiv \mathbf{u}^{+}(x,y;z \to +0) - \mathbf{u}^{-}(x,y;z \to -0) = \begin{bmatrix} u_x^{+} - u_x^{-} \\ u_y^{+} - u_y^{-} \\ u_z^{+} - u_z^{-} \end{bmatrix}, \quad (3)$$

$$\boldsymbol{\sigma}^{\pm}(x,y) \equiv \boldsymbol{\sigma}^{\pm}(x,y;z \to \pm 0) = \begin{bmatrix} \sigma_{xz}^{\pm} \\ \sigma_{yz}^{\pm} \\ \sigma_{zz}^{\pm} \end{bmatrix}, \quad \boldsymbol{\sigma}(x,y) \equiv \begin{bmatrix} \sigma_{xz} \\ \sigma_{yz} \\ \sigma_{zz} \end{bmatrix}, \quad (4)$$

$$\boldsymbol{\eta}(x,y) \equiv \begin{bmatrix} \eta_{xx} & \eta_{xy} & \eta_{xz} \\ \eta_{yx} & \eta_{yy} & \eta_{yz} \\ \eta_{zx} & \eta_{zy} & \eta_{zz} \end{bmatrix}, \quad (5)$$

where the superscripts "$^-$" and "$^+$" indicate the two sides of the fracture. Since we use only the three stress components on the *x*,*y* plane, the stress can be treated as a three-component, traction vector instead of a six-compoent tensor. We assume that the incident waves insonify the fracture on the "$^-$" side. By directly applying the spatial 2D Fourier transform to these "local" SDD conditions,

$$\tilde{\boldsymbol{\sigma}}^+(k_x,k_y) = \tilde{\boldsymbol{\sigma}}^-(k_x,k_y) \equiv \tilde{\boldsymbol{\sigma}}(k_x,k_y), \quad (6)$$

$$\left(\tilde{\boldsymbol{\eta}} * \tilde{\boldsymbol{\sigma}}\right)(k_x,k_y) = \left[\tilde{\mathbf{u}}\right](k_x,k_y). \quad (7)$$

Tilde "$\tilde{}$" indicates transformed variables, and "*" indicates a convolution. It is noted that for a uniform fracture, $\boldsymbol{\eta}(x,y)$ is a constant matrix, and the convolution is reduced to a multiplication, i.e., the same relationship as in the *x*, *y* domain.

As shown in Appendix A, in the wavenumber domain, the displacement and stress can be related to each other via single vector variables $\mathbf{a}^{\pm}$ containing the displacement amplitudes of three plane wave modes (for isotropically elastic media, these are one compressional wave and two shear waves). Therefore, for each wavenumber component, the above equations are rewritten respectively as

$$\mathbf{S}^+\mathbf{a}^+ = \mathbf{S}^-\mathbf{a}^- + \mathbf{S}^+\mathbf{a}_{Inc} \equiv \tilde{\boldsymbol{\sigma}}(k_x,k_y), \quad (8)$$

$$\tilde{\boldsymbol{\eta}} * \left(\mathbf{S}^+\mathbf{a}^+\right) = \mathbf{U}^+\mathbf{a}^+ - \mathbf{U}^-\mathbf{a}^- - \mathbf{U}^+\mathbf{a}_{Inc}. \quad (9)$$

The 3×3 matrices $\mathbf{U}^{\pm}$ (displacement matrices), and $\mathbf{S}^{\pm}$ (stress matrices) are defined in the Appendix A. $\mathbf{a}_{Inc}$ is the amplitude vector for the incident wave. The superscript "^{T}" indicates the vector and matrix transposition. Also, hereafter, the superscripts "$^-$" and "$^+$" indicate waves propagating in the negative *z* direction (reflected waves) and in the positive *z* direction (incident

and transmitted waves). To simplify the above equations, we choose to use the stress vector $\tilde{\boldsymbol{\sigma}}$ as our primary variable. This choice leads to an efficient implementation of a numerical algorithm, which we will discuss later. Using the equalities in the first equation, the variables $\mathbf{a}^-$ (reflected waves) and $\mathbf{a}^+$ (transmitted waves) are eliminated from the second equation, resulting in

$$\left(\mathbf{H} - \tilde{\boldsymbol{\eta}}^*\right)\tilde{\boldsymbol{\sigma}} = \mathbf{H}\tilde{\boldsymbol{\sigma}}_{Inc}, \quad (10)$$

where

$$\mathbf{H} \equiv \mathbf{U}^+\left(\mathbf{S}^+\right)^{-1} - \mathbf{U}^-\left(\mathbf{S}^-\right)^{-1}. \quad (11)$$

Also, the stress introduced by the incident wave is given by $\tilde{\boldsymbol{\sigma}}_{Inc} = \mathbf{S}^+\mathbf{a}_{Inc}$. Eq.(10) is a Fredholm integral equation of the 2nd kind

$$\tilde{\boldsymbol{\sigma}}(k_x, k_y) = \tilde{\boldsymbol{\sigma}}_{Inc}(k_x, k_y) + \mathbf{H}^{-1}(k_x, k_y)\int_{-\infty}^{+\infty}\int_{-\infty}^{+\infty}\tilde{\boldsymbol{\eta}}(k_x - k_x', k_y - k_y')\tilde{\boldsymbol{\sigma}}(k_x', k_y')dk_x'dk_y'. \quad (12)$$

The first term on the right hand side of the equation is the incident wave field, and the second term is the scattered wave field. The second term shows that, for a heterogeneous fracture compliance distribution, different wavenumber components are coupled through the convolution with the Fourier transformed fracture compliance, resulting in non-specular transmission and reflection of an incident plane wave. For simplicity, we define matrix operators $\bar{\mathbf{H}}^{-1}$ and $\bar{\tilde{\boldsymbol{\eta}}}$. These operators perform multiplication with the matrix $\mathbf{H}^{-1}$ and convolution with the matrix $\tilde{\boldsymbol{\eta}}$, respectively, on a vector function. The formal solution of Eq.(12) is obtained (Neumann series) by first introducing these operators as

$$\tilde{\boldsymbol{\sigma}} = \tilde{\boldsymbol{\sigma}}_{Inc} + \bar{\mathbf{H}}^{-1}\bar{\tilde{\boldsymbol{\eta}}}\tilde{\boldsymbol{\sigma}} \equiv \tilde{\boldsymbol{\sigma}}_{Inc} + i\bar{\boldsymbol{\Omega}}\tilde{\boldsymbol{\sigma}}, \quad (13)$$

where $i\bar{\boldsymbol{\Omega}} \equiv \bar{\mathbf{H}}^{-1}\bar{\tilde{\boldsymbol{\eta}}}$, and then by applying Eq.(13) recursively to itself as

$$\tilde{\boldsymbol{\sigma}} = \left[\bar{\mathbf{I}} + i\bar{\boldsymbol{\Omega}} + (i\bar{\boldsymbol{\Omega}})^2 + ... \right] \tilde{\boldsymbol{\sigma}}_{Inc} = \left(\bar{\mathbf{I}} - i\bar{\boldsymbol{\Omega}} \right)^{-1} \tilde{\boldsymbol{\sigma}}_{Inc} . \qquad (14)$$

$\bar{\mathbf{I}}$ is the identity operator. If the scattering is weak so that the stress field on the fracture can be approximated by the stress introduced by the incident wave, the (1st-order) Born approximation can be used in Eq.(13), resulting in

$$\tilde{\boldsymbol{\sigma}} = \tilde{\boldsymbol{\sigma}}_{Inc} + i\bar{\boldsymbol{\Omega}}\tilde{\boldsymbol{\sigma}}_{Inc} = \left(\bar{\mathbf{I}} + i\bar{\boldsymbol{\Omega}} \right) \tilde{\boldsymbol{\sigma}}_{Inc} , \qquad (15)$$

which can also be obtained by keeping the first two terms in the Neumann series (Born series) in Eq.(14). It is noted that an alternative approximation that is valid for the strong-scattering limit can be obtained if the stiffness of the fracture, instead of compliance, is used. The derivation of this approximation is shown in Appendix B.

Introducing higher-order terms in the Born series increases the applicable range of the approximation for stronger scattering, as long as the series is convergent. However, the series may converge very slowly, or even may not converge for moderately to strongly scattering fractures (for weakly to moderately scattering fractures if the formulation in Appendix B is used). For these cases, the original system equation (10) has to be solved numerically.

B. Numerical analysis

In order to solve the integral equation (12) numerically, the equation is discretised to obtain a linear system of equations by applying the discrete Fourier transforms instead of the continuous Fourier transforms. This indicates that both the two-dimensional fracture compliance distribution and the resulting waves are treated as periodic, though the waves can be periodic in the dynamic sense as in the Floquet boundary condition (i.e., a constant phase shift is included in the periodic boundary condition). Also, for the linear system of equation to be finite in size, the spectra of the transformed fracture compliance need to be band limited (decay away from the origin sufficiently fast). The discrete form of the Eq.(10) is (for computational efficiency, Eqs.(12) and (13) are not used)

$$\sum_{m'=0}^{M-1}\sum_{n'=0}^{N-1}\left[\delta_{mm'}\delta_{nn'}\mathbf{H}_{mn}-\tilde{\boldsymbol{\eta}}_{m-m',n-n'}\right]\tilde{\boldsymbol{\sigma}}_{m'n'}=\mathbf{H}_{mn}\tilde{\boldsymbol{\sigma}}_{Inc,mn}\,. \qquad (17)$$

$(m=0,1,...,M-1 \text{ and } n=0,1,...,N-1)$

$\delta_{mm'}$ and $\delta_{nn'}$ are Kronecker deltas. All vectors and matrices are evaluated at discrete wavenumbers $(k_{xm},k_{yn})=(2m\pi/L_x,2n\pi/L_y)$ and indicated by indices (m, n). Note that all these indices are periodic with a period (M, N), and the compliance distribution is spatially periodic with a period (L_x, L_y). The length of the period (M, N) should be sufficiently long to avoid spectral leakage in the solution. By grouping the two indices (m, n) and (m', n') to the vectors and matrices into single indices l and l' (l, l'=0, 1, …, MN-1), respectively, Eq.(17) are assembled into a single matrix equation

$$\left(\bar{\mathbf{H}}-\bar{\tilde{\boldsymbol{\eta}}}\right)\bar{\boldsymbol{\sigma}}=\bar{\mathbf{H}}\bar{\boldsymbol{\sigma}}_{Inc}\,, \qquad (18)$$

where

$$\bar{\mathbf{H}}\equiv\begin{bmatrix}\mathbf{H}_0 & & & \\ & \mathbf{H}_1 & & \\ & & \ddots & \\ & & & \mathbf{H}_{MN-1}\end{bmatrix},\ \bar{\tilde{\boldsymbol{\eta}}}\equiv\begin{bmatrix}\tilde{\boldsymbol{\eta}}_0 & \tilde{\boldsymbol{\eta}}_{-1} & \cdots & \tilde{\boldsymbol{\eta}}_{-MN+1}\\ \tilde{\boldsymbol{\eta}}_{+1} & \tilde{\boldsymbol{\eta}}_0 & \cdots & \tilde{\boldsymbol{\eta}}_{-MN+2}\\ \vdots & \vdots & \ddots & \vdots\\ \tilde{\boldsymbol{\eta}}_{MN-1} & \tilde{\boldsymbol{\eta}}_{MN-2} & \cdots & \tilde{\boldsymbol{\eta}}_0\end{bmatrix},$$

$$\bar{\boldsymbol{\sigma}}=\begin{bmatrix}\tilde{\boldsymbol{\sigma}}_0\\ \tilde{\boldsymbol{\sigma}}_1\\ \vdots\\ \tilde{\boldsymbol{\sigma}}_{MN-1}\end{bmatrix},\ \bar{\boldsymbol{\sigma}}_{Inc}=\begin{bmatrix}\tilde{\boldsymbol{\sigma}}_{Inc,0}\\ \tilde{\boldsymbol{\sigma}}_{Inc,1}\\ \vdots\\ \tilde{\boldsymbol{\sigma}}_{Inc,MN-1}\end{bmatrix}. \qquad (19)$$

Once the stress vector $\bar{\boldsymbol{\sigma}}$ is determined, by solving Eq.(18), the coefficient vectors for each wavenumber and wave mode component are computed via

$$\mathbf{a}_{mn}^{+}=\left(\mathbf{S}_{mn}^{+}\right)^{-1}\tilde{\boldsymbol{\sigma}}_{mn}\,, \qquad (20)$$

$$\mathbf{a}^{-}_{mn} = \left(\mathbf{S}^{-}_{mn}\right)^{-1}\left(\tilde{\boldsymbol{\sigma}}_{mn} - \tilde{\boldsymbol{\sigma}}_{Inc}\right), \qquad (21)$$

for transmitted and reflected waves, respectively. From these, the displacement vectors for the transmitted and reflected waves are

$$\mathbf{u}^{+}(x, y, z > 0) = \sum_{m=0}^{M-1}\sum_{n=0}^{N-1} \mathbf{U}^{+}_{mn}\mathbf{E}^{+}_{mn}\mathbf{a}^{+}_{mn} e^{i(k_{xm}x + k_{yn}y - \omega t)}, \qquad (22)$$

$$\mathbf{u}^{-}(x, y, z < 0) = \sum_{m=0}^{M-1}\sum_{n=0}^{N-1} \left(\mathbf{U}^{-}_{mn}\mathbf{E}^{-}_{mn}\mathbf{a}^{-}_{mn} + \mathbf{U}^{+}_{mn}\mathbf{E}^{+}_{mn}\mathbf{a}_{Inc,mn}\right) e^{i(k_{xm}x + k_{yn}y - \omega t)}, \qquad (23)$$

where $\mathbf{E}^{\pm}_{mn} = \mathbf{E}^{\pm}(k_{mx}, k_{ny}; z)$ are the discrete forms of the phase-shift matrices defined in Appendix A.

C. Computational considerations

The system matrix has a size (M_{mat}×M_{mat}) where M_{mat}=M×N×DOF (degrees of freedom, three for three-dimensional problems) which grows rapidly as the number of wavenumber components increases. However, unique properties of the equation allow an efficient implementation of the method in a computer program, which leads to significant savings in the computer time and memory.

First, we discuss the memory considerations. From Eqs.(17) and (18), it is noticed that the system matrix consists of two parts: the 3×3 block diagonal part $\bar{\mathbf{H}}$, and the fully populated part $\bar{\tilde{\boldsymbol{\eta}}}$. The latter matrix has the same structure as the Toeplitz matrix: each element of the matrix, a 3×3 submatrix, appears recursively, with the first entry of the compliance matrix $\tilde{\boldsymbol{\eta}}_{00} = \tilde{\boldsymbol{\eta}}_{0}$ in the diagonal. Therefore, for this system matrix, if an iterative solver such as the stabilized bi-conjugate gradient method (Van der Vorst, 1994) or the GMRES method (Saad and Schultz, 1986) is used, it is sufficient to store only the block diagonal part of the matrix $\bar{\mathbf{H}}$ and the transformed fracture compliance matrices corresponding to the first 3×M_{mat} part of the matrix $\bar{\tilde{\boldsymbol{\eta}}}$.

An iterative solver requires both fast computation of matrix-vector products (mat-vecs) and effective preconditioning of the system matrix. The fully populated structure of the system matrix is usually not suited for fast computation of mat-vecs. Fortunately, Eq.(17) reveals that the matrix-vector product between $\bar{\bar{\tilde{\boldsymbol{\eta}}}}$ and $\bar{\tilde{\boldsymbol{\sigma}}}$ is essentially a single convolution between $\tilde{\boldsymbol{\eta}}_{m,n}(=\tilde{\boldsymbol{\eta}}_l)$ and $\tilde{\boldsymbol{\sigma}}_{m,n}(=\tilde{\boldsymbol{\sigma}}_l)$. Therefore, this computation can be carried out efficiently by transforming the vectors to the spatial domain and then transforming back the products between the vectors and the local compliance matrices to the wavenumber domain, using Fast Fourier Transforms. The preconditioning of the matrix is carried out in the spatial domain using the Kirchhoff approximation of the scattered waves.

Finally, for a plane incident wave with a wavenumber vector (k_x^{Inc}, k_y^{Inc}), the definition of the wavenumbers is changed to $(k_{xm}, k_{yn}) = (k_x^{Inc} + 2m\pi / L_x, k_y^{Inc} + 2n\pi / L_y)$, so that the non-specular wavenumber components close to the incident wave wavenumber are preferentially used to represent the scattered waves. This is a reasonable choice because the partial waves with wavenumbers close to the source wavenumber are more strongly excited due to the coupling introduced by the diagonally dominant kernel of the convolution integral in Eq.(12). The expression for the stress vector also changes as

$$\tilde{\boldsymbol{\sigma}}_{Inc,mn} \rightarrow \delta_{m0}\delta_{n0}\tilde{\boldsymbol{\sigma}}_{Inc}, \quad (24)$$

III. EXAMPLES

A. Comparison with a boundary element code

In order to check the performance of the numerical technique, we compared the numerical results of the wd-SDD technique developed in the previous sections to the results from a two-dimensional, frequency-domain elastodynamic boundary element (BE) method of Hirose and Kitahara (1991). In this test, the results from the two methods were compared for plane waves propagating along the *x*, *z* plane. We assumed a fracture with sinusoidal compliance distribution in the *x* direction as shown in Figure 2, and a plane wave normally incident on the fracture. In

contrast to the three-dimensional, infinitely periodic model used in the wd-SDD technique, the two-dimensional fracture in the BE model is finite in its extent (56 m long).

z-direction particle motions of the waveforms computed for receivers located on both sides of the fracture are shown in Figure 3. The distance of the receivers from the fracture is 20 m, the incident wave is a plane P wave Ricker wavelet (second derivative of a Gaussian wavelet) with a central frequency corresponding to 4 m which is also the length period of the compliance distribution. Compared to the SDD results, the BE results show much shorter, more compact waveforms, because the fracture in the BE model is finite. The initial part of the waveforms, however, show very good agreement for both reflected and transmitted fractures, which indicates that the scattering of the waves can be accurately modeled using the wavenumber-domain SDD technique. The secondary arrivals that also show rather good agreement are due to the S waves converted by the fracture.

B. Numerical models of a heterogeneous fracture

In the following examples, we used a fracture with a numerically simulated stochastic compliance distribution. For simplicity, the fracture compliance matrix was assumed to be proportional to an identity matrix, i.e., normal and shear compliances are the same, and $\boldsymbol{\eta}(x, y) = \eta(x, y)\mathbf{I}$. A distribution of logarithmic compliance, $ln\ \eta(x, y)$, was generated from a Gaussian correlation function with a correlation length (one standard deviation) of 4 m and uncorrelated phase between the Fourier components (Pardo-Iguzquiza and Chica-Olmo, 1993). The range of a single periodic cell is (L_x, L_y)=(64 m, 64 m). The resulting compliance $\eta(x, y)$, shown in Figure 4, has a log-normal distribution with a mean and a standard deviation of the compliance of 6.74×10^{-11} m/Pa and 4.87×10^{-11} m/Pa, respectively. The correlation length of the distribution (one standard deviation of a fitted Gaussian profile) is approximately 4 m.

C. Exact solutions

Waves scattered by the heterogeneous fracture in Figure 4 were computed for a plane incident P wave, using a Ricker wavelet (2^{nd} derivative of a Gaussian function) with a central frequency, 750 Hz, corresponding to the correlation length of the fracture. The velocities and density of the

homogeneous, isotropic, elastic background were c_p=3000 m/s, c_s=1731 m/s, and ρ=2100 kg/m^3, respectively. If the fracture had a homogeneous fracture compliance distribution, the mean compliance value of 6.74×10^{-11} m/Pa would give the same P wave transmission and reflection coefficients of 0.71.

The snapshots in Figure 5a and 5b were computed for both normally incident wave and obliquely incident wave with a propagation vector (v_x,v_y, v_z)=(1, 1, 1), respectively. To emphasize the scattered waves with small amplitudes, the amplitude scale was magnified by a factor of 4, which caused the saturation of scale for a part of transmitted and reflected waves. In both snapshots, it can be seen that patches of large and small compliance scatter the incident waves, creating circular (spherical) diffraction patterns in both sides of the fracture. For the normal incidence case, the amplitude and phase fluctuations in the both transmitted and reflected waves can be seen. It is also noted that incoherent plane *S* waves were generated. For the oblique incidence case, the diffracted waves generated horizontally propagating nearly plane *P* waves in later times, part of which is critically refracted as head waves propagating away from the fracture (multiple, faint oblique wave fronts propagating symmetrically across the fracture).

Figure 6 shows the amplitude distribution of individual wavenumber components for a given frequency (750 Hz) and angles of incidence (normal and oblique) of incident plane *P* waves. The axes of the plots show the integral numbers (*m*, *n*) corresponding to the wavenumber components $(k_{xm}, k_{yn}) = (k_x^{Inc} + 2m\pi / L_x, k_y^{Inc} + 2n\pi / L_y)$. It is reminded that the components of wavenumbers used in the numerical simulations were distributed around the incident wavenumber (k_x^{Inc}, k_y^{Inc}). These diagrams can be used to see if the spectrum leakage occurs due to a premature truncation of the wavenumber series (or undersampling in the spatial domain). For this example, although the length of the wavenumber series was rather short ((M, N)=(32, 32)), the amplitudes of the scattered waves became significantly small at the edge of the diagram, showing *a posteori* that the selected length of the series was sufficiently long. It is also noted that while normal-incidence case showed no coupling between the incident *P* wave and *Sh* waves, the oblique-incidence case showed small *Sh* waves.

D. Born approximations and low and high-frequency asymptotic solutions

If the compliance distribution is uniform, only the specular wavenumber component needs to be examined. This is because the convolution matrix, $\bar{\tilde{\boldsymbol{\eta}}}$, and therefore the system matrix in Eq. (18), becomes block diagonal due to the lack of coupling between different wavenumber components. For a plane incident wave, using the vectors and matrices in Eq.(19), the "exact" equation (18) reduces to

$$\left(\mathbf{H}_0 - \tilde{\boldsymbol{\eta}}_0\right)\tilde{\boldsymbol{\sigma}} = \mathbf{H}_0\tilde{\boldsymbol{\sigma}}_{Inc} \text{ or } (\mathbf{I} - \mathbf{H}_0^{-1}\tilde{\boldsymbol{\eta}}_0)\tilde{\boldsymbol{\sigma}}_0 \equiv (\mathbf{I} - i\boldsymbol{\Omega}_0)\tilde{\boldsymbol{\sigma}}_0 = \tilde{\boldsymbol{\sigma}}_{Inc}. \quad (25)$$

For a diagonal fracture compliance matrix $\tilde{\boldsymbol{\eta}}_0 \equiv diag\left[\eta_{xx}, \eta_{yy}, \eta_{zz}\right]$, $\boldsymbol{\Omega}_0$ is

$$\begin{aligned}\boldsymbol{\Omega}_0 &= Diag\left[\frac{\omega\rho c_S\eta_{xx}}{2} \quad \frac{\omega\rho c_S\eta_{yy}}{2} \quad \frac{\omega\rho c_P\eta_{zz}}{2}\right]. \quad (26)\\ &\equiv Diag\left[\Omega_{Sv} \quad \Omega_{Sh} \quad \Omega_P\right]\end{aligned}$$

The components of the matrix are the dimensionless frequencies defined by Haugen and Schoenberg (2000). The stiffness based equations (Appendix B) also reduces to

$$\left(\mathbf{H}_0^{-1} - \tilde{\boldsymbol{\kappa}}_0\right)[\tilde{\mathbf{u}}] = \mathbf{H}_0^{-1}[\tilde{\mathbf{u}}]_{Inc} \text{ or } (\mathbf{I} - \mathbf{H}_0\tilde{\boldsymbol{\kappa}}_0)[\tilde{\mathbf{u}}]_0 \equiv (\mathbf{I} + i\mathbf{T}_0\tilde{\boldsymbol{\kappa}}_0)[\tilde{\mathbf{u}}]_0 = [\tilde{\mathbf{u}}]_{Inc}. \quad (27)$$

Since both $\tilde{\boldsymbol{\eta}}_0$ and $\tilde{\boldsymbol{\kappa}}_0$ are constant and diagonal, and $\mathbf{H}_0$ is also diagonal for normally incident waves, $\tilde{\boldsymbol{\kappa}}_0 = \tilde{\boldsymbol{\eta}}_0^{-1}$, and $\mathbf{T}_0 = \boldsymbol{\Omega}_0^{-1}$. Therefore, the two Born series are

$$\tilde{\boldsymbol{\sigma}}_0 = \sum_{n=0}^{\infty} i^n \boldsymbol{\Omega}_0^{\,n} \cdot \tilde{\boldsymbol{\sigma}}_{Inc} \quad (28)$$

$$[\tilde{\mathbf{u}}]_0 = \sum_{n=0}^{\infty} (-i)^n \boldsymbol{\Omega}_0^{-n} \cdot [\tilde{\mathbf{u}}]_{Inc}. \quad (29)$$

Since the eigenvalues of the matrices $\boldsymbol{\Omega}_0$ and $\boldsymbol{\Omega}_0^{-1}$ are the Haugen and Schoenberg's dimensionless frequencies and their inverse, the above Born series converge for $\left|\Omega_{Sv,Sh,P}\right| < 1$ for compliance based series, and $\left|\Omega_{Sv,Sh,P}\right| > 1$ for the stiffness based series. Therefore compliance

and stiffness based Born approximations can be applied in the low and high frequency limits, respectively.

For heterogeneous fracture compliance and stiffness distributions, these relationships are more complicated due to the non-specular scattering of waves. The matrix-vector form of the Born series is obtained from Eq.(18) as

$$\bar{\boldsymbol{\sigma}} = \sum_{n=0}^{\infty} \left(\bar{\mathbf{H}}^{-1} \bar{\tilde{\boldsymbol{\eta}}} \right)^n \bar{\boldsymbol{\sigma}}_{Inc} \equiv \sum_{n=0}^{\infty} i^n \bar{\boldsymbol{\Omega}}^n \bar{\boldsymbol{\sigma}}_{Inc} \ . \qquad (30)$$

Also, from Appendix B, the stiffness based Born series is

$$[\bar{\mathbf{u}}] = \sum_{n=0}^{\infty} \left(\bar{\mathbf{H}} \bar{\tilde{\boldsymbol{\kappa}}} \right)^n [\bar{\mathbf{u}}]_{Inc} \equiv \sum_{n=0}^{\infty} (-i)^n \bar{\mathbf{T}}^n [\bar{\mathbf{u}}]_{Inc} \ . \qquad (31)$$

These series are convergent if $\left\| \bar{\boldsymbol{\Omega}} \right\| < 1$ and $\left\| \bar{\mathbf{T}} \right\| < 1$, i.e., the magnitude of the eigenvalues of the matrices are smaller than unity. It is desirable to interpret these conditions as the low and high-frequency limits, as we saw for a homogeneous fracture, so that we can apply the Born approximations to the low and high-frequency scattering problems for a heterogeneous fracture. We will examine these possibilities using numerical simulations.

For the fracture model used in the previous section, we can compute the scattered wavefield from the (generalized) Born series. For simplicity, we assume normally incident, monochromatic transmitted *P* waves, and examine only the specular component of the waves. The "exact" solutions are also computed from Eq.(18) for a range of frequencies, and compared to the Born approximations of different orders. Figure 7a and 7b show the comparisons of transmission coefficient amplitudes computed from the *z*-direction particle motions of *P* waves. Each curve in the plots is labeled with the order of Born approximation. The low-frequency approximations were computed using the compliance-based Born series, and the high-frequency approximations were computed using the stiffness-based Born series. As can be seen from the plots, the both Born approximations appear to be valid in the low and high-frequency limits, respectively, and including higher-order terms in the Born series does improve the applicability of the approximations. In Figure 8, *z*-direction particle motions are compared for both 3rd –order Born

approximation and the exact numerical solution. The receivers are located at z=32 m (transmitted waves) and z=–32 m (reflected waves), and a low frequency (a central frequency of 100 Hz) Ricker wavelet was used. For this example, the results of the two methods are indistinguishable.

However, these results do not necessarily guarantee that the first two terms in the Born series (first-order Born approximations) are exactly the leading terms in the series, i.e., low and high-frequency asymptotes of the exact solutions. We examined the low and high-frequency limit behavior of the two Born series more in detail by plotting the amplitudes of individual terms' contribution as a function of frequency (Figure 9a and 9b, respectively).

From Figure 9a, the second and the higher-order terms of the Born series all exhibit $o(\omega)$-dependence, instead of the expected $o(\omega^n)$-dependence for a homogeneous fracture in Eq.(28), where n is the order of the term. This indicates that, although it is still a good approximation due to small magnitudes of the terms higher than n>2, the lowest-order, compliance-based Born approximation does not give the exact low-frequency asymptotic solution. In contrast, from Figure 9b, the higher-order terms in the stiffness-based Born approximation are of the order $o(1/\omega^{n+1})$. Therefore, the Born series give correct high-frequency asymptotes.

IV. CONCLUSIONS

We developed a plane wave method to compute the three-dimensional scattering of plane elastic waves by a fracture with a heterogeneous stiffness (compliance) distribution. This technique allows us to examine the relationships between the characteristics of scattered elastic waves and the microstructural variations along the fracture plane, e.g., surface contact and crack distribution, gouge layer thickness variation, that are modeled as heterogeneities in the fracture compliance distribution.

This method is a straightforward extension of the commonly used seismic displacement discontinuity (SDD) method for a homogeneous fracture, to a fracture with a heterogeneous fracture compliance distribution. Even though the developed technique is a full-waveform technique and successfully models a variety of wave phenomena involving a fracture, such as

mode converted waves, head waves (refracted waves), surface waves and diffracted waves, it does not require massive parallel computers as finite difference methods and boundary element methods would do. All examples given in this paper were computed using a small, single processor desk-top computer with a limited amount of memory and speed (200 MB RAM and 400 MHz clock speed).

The current numerical technique can be applied to non-planar incident waves by simply modifying the incident wave vector. In this case, however, a larger number of wavenumber components need to be used in the matrix equation. It should also be noted that this technique is difficult to apply to extremely heterogeneous fractures, because such fractures typically results in a large linear system of equations to solve for non-specular components of scattered waves with wavenumbers far different from the incident wave. Further, the compliance-based equations break down for open cracks and voids (infinite compliance) and the stiffness-based equations break down for welded surfaces (infinite stiffness), because the Fourier transforms cannot be performed.

Lastly, we demonstrated that two types of Born series can be used to examine the low and high-frequency limit behavior of the wave scattering by a heterogeneous fracture. The low-frequency Born series (compliance-based formulation), however, should be used with a caution, because the lowest-order term does not provide the exact low-frequency asymptotic solution. In contrast, the high-frequency Born series (stiffness-based formuation) is the exact high-frequency asymptote, although, in practice, the local SDD conditions used as a basis of the theory may not be valid for such high frequencies.

ACKNOWLEDGMENTS

This research has been supported by the Office of Science, Office of Basic Energy Sciences, Division of Chemical Sciences of the U.S. Department of Energy under contract No. DE-AC76SF00098.

REFERENCES

[1] Liu, E., J.A. Hudson, and T. Pointer, 2000, Equivalent medium representation of fractured rock, *J. Geophys. Res.*, **105**(B2), 2981-3000.

[2] Schoenberg, M.A., 1980, Elastic wave behavior across linear slip interfaces, *J. Acoust. Soc. Am.*, **68**, 1516-1521.

[3] Baik, J. and R.B. Thompson, 1984, Ultrasonic scattering from imperfect interfaces: a quasi-static model, *J. Nondestruct. Eval*., **4**, 177-196.

[4] Angel, Y.C. and J.D. Achenbach, 1985, Reflection and transmission of elastic waves by a periodic array of cracks, *J. Appl. Mech.*, **52**, 33-41.

[5] Myer, L.R., D. Hopkins and N.G.W. Cook, 1985, Effects of contact area of an interface on acoustic wave transmission, in Proc. 26th US Symp. on Rock Mech., 549-556.

[6] Pyrak-Nolte, L.J. and N.G.W. Cook, 1987, Elastic interface waves along a fracture, *Geophys. Res. Lett.*, **14(**11**)**, 1107-1110.

[7] Rockhlin, S.I. and Y.J. Wang, 1991, Analysis of boundary conditions for elastic wave interaction with an interface between two solids, *J. Acoust. Soc. Am*., **89**(2)

[8] Nakagawa, S., K. T. Nihei, and L. R. Myer, 2002, Elastic wave propagation along a set of parallel fractures, *Geophys. Res. Lett*, AGU DOI: 10.1029/2002GL014925.

[9] Pyrak-Nolte, L.J., L.R. Myer, N.G.W. Cook, and P.A. Witherspoon, 1987, Hydraulic and mechanical properties of natural fractures in low permeability rock, in Proceedings of the 6th International Congress of Rock Mechanics, Montreal, I, 225-232.

[10] Buck, O., D.K. Rehbein, and R.B. Thompson, 1987, Crack tipshielding by asperity contact as determined by acoustic measurements, *Eng. Frac. Mech.*, **28**(4), 413-424.

[11] Jones, G. and R.J. Knipe, 1996, Seismic attribute maps: Application of structural interpretation and fault seal analysis in the North Sea basin, *First Break*, **12**, 449-461.

[12] Hakami, E. and E. Larsson, 1996, Aperture measurement and flow experiments on a single natural fracture, *Int. J. Rock Mech. Min Sci. Geomech. Abstr*., **33**(4), 395-404.

[13] Pyrak-Nolte, L.J. and D.D. Nolte, 1992, Frequency dependence of fracture stiffness, *Geophys. Res. Lett*., **19**(3), 325-328.

[14] Nihei, K.T., 1989, *Modeling Elastic Waves in Fractured Rock with the Kirchhoff Method*, M.S. Thesis, University of California at Berkeley.

[15] Oliger, A., L.J. Pyrak-Nolte, and D.D. Nolte, 2003, Seismic focusing by a single planar fracture, to appear in *Geophys. Res. Lett*.

[16] Mikata, Y. and J.D. Achenbach, 1988, Interaction of harmonic waves with a periodic array of inclined cracks, *Wave Motion*, **10**, 59-72.

[17] Punjani, M. and L.J. Bond, 1986, Scattering of plane waves by a partially closed crack, *Review of Progress in Quant. Nondestruct. Eval.*, **5A**, Punjanni and Bond, 61-71.

[18] Coates, R.T. and Schoenberg, M.A., 1995, Finite-difference modeling of faults and fractures, *Geophysics*, **60**, 1514-1526.

[19] Van der Vorst, H., 1992, Bi-CGSTAB: A fast and smoothly converging variant of Bi-CG for the solution of nonsymmetric linear equations, *SIAM, J. Sci. Stat. Comput*., **13**, 631-644.

[20] Saad, Y. and M.H. Schultz, 1986, GMRES: A generalized minimum residual algorithm for solving unsymmetric linear systems, *SIAM, J. Sci. Stat. Comput*., **7**, 856-869.

[21] Hirose, S. and M. Kitahara, 1991, Scattering of elastic waves by a crack with spring-mass contact, *Int. J. Num. Meth. Engng.*, **31**, 789-801.

[22] Pardo-Iguzquiza, E. and M. Chica-Olmo, 1993, The Fourier Integral Method: An efficient spectral method for simulation of random fields, *Mathematical Geology*, **25**(2), 177-217.

[23] Haugen, G.U. and M.A. Schoenberg, 2000, The echo of a fault or fracture, *Geophysics*, **65**(1), 176-189.

APPENDIX A

We assume a single plane fracture embedded within a homogeneous background medium with a stiffness tensor $\mathbf{C}=[C_{ijkl}]$ and a density ρ. It is also assumed that the fracture plane is on the z=0 plane in the Cartesian coordinate system. For a given frequency ω and plane-parallel wavenumbers k_x and k_y, the Christoffel equation is solved to obtain six z-direction wavenumbers $k_z^{1\pm}$, $k_z^{2\pm}$, $k_z^{3\pm}$, and corresponding unit particle displacement vectors $\hat{\mathbf{u}}_1^{\pm}$, $\hat{\mathbf{u}}_2^{\pm}$, $\hat{\mathbf{u}}_3^{\pm}$. Using these wavenumbers and vectors, plane wave displacement is given by

$$\begin{aligned}\mathbf{u}^{\pm}(x,y,z) &= \begin{bmatrix} u_x^{\pm} \\ u_y^{\pm} \\ u_z^{\pm} \end{bmatrix} = \begin{Bmatrix} \hat{\mathbf{u}}_1^{\pm} & \hat{\mathbf{u}}_2^{\pm} & \hat{\mathbf{u}}_3^{\pm} \end{Bmatrix} \begin{bmatrix} e^{ik_z^{1\pm}z} & & \\ & e^{ik_z^{2\pm}z} & \\ & & e^{ik_z^{3\pm}z} \end{bmatrix} \begin{bmatrix} a_1^{\pm} \\ a_2^{\pm} \\ a_3^{\pm} \end{bmatrix} e^{i(k_x x + k_y y - \omega t)} \\ &= \mathbf{U}^{\pm}(k_x,k_y)\mathbf{E}^{\pm}(k_x,k_y;z)\mathbf{a}^{\pm}(k_x,k_y)e^{i(k_x x + k_y y - \omega t)}\end{aligned} \quad . \qquad \text{(A1)}$$

The stress is computed from the displacement vector using the Hooke's law $\boldsymbol{\tau}^{\pm} \equiv \left[\sigma_{ij}^{\pm}\right] = \mathbf{C} : \nabla \mathbf{u}^{\pm}$. Since we consider only the stress components on the z plane, we define a stress vector by

$$\begin{aligned}\boldsymbol{\sigma}^{\pm}(x,y,z) &= \begin{bmatrix} \sigma_{xz}^{\pm} \\ \sigma_{yz}^{\pm} \\ \sigma_{zz}^{\pm} \end{bmatrix} \\ &= \mathbf{S}^{\pm}(k_x,k_y)\mathbf{E}^{\pm}(k_x,k_y;z)\mathbf{a}^{\pm}(k_x,k_y)e^{i(k_x x + k_y y - \omega t)}\end{aligned} \quad . \qquad \text{(A2)}$$

For an isotropic background medium, the three modes of wave propagation is two shear (S) waves and one compressional (P) wave. We label these modes as 1=*Sv* wave, 2=*Sh* wave, and 3=*P* wave, where a convention is taken such that the *Sh* wave has the particle displacement parallel to the fracture (or z) plane. The z-direction wavenumbers are $k_z^{1,2\pm} = \pm k_z^S \equiv \pm\sqrt{k_S^2 - k_r^2}$ and $k_z^{3\pm} = \pm k_z^P \equiv \pm\sqrt{k_P^2 - k_r^2}$, where $k_r = \sqrt{k_x^2 + k_y^2}$ with P and S-wave wavenumbers k_P and k_S, respectively. The displacement and stress matrices in Eqs.(A.1) and (A.2) take the forms

$$\mathbf{U}^{\pm} = \mathbf{R}^T \begin{bmatrix} \mp k_z^S / k_S & & k_r / k_P \\ & 1 & \\ k_r / k_S & & \pm k_z^P / k_P \end{bmatrix}, \quad \text{(A3)}$$

$$\mathbf{S}^{\pm} = i\omega\rho c_S \mathbf{R}^T \begin{bmatrix} -(1-2(k_r / k_S)^2) & 0 & \pm 2k_r k_z^P / k_P k_S \\ 0 & \pm k_z^S / k_S & 0 \\ \pm 2k_r k_z^S / k_S^2 & 0 & (1-2(k_r / k_S)^2)(k_S / k_P) \end{bmatrix}, \text{(A4)}$$

where c_S is the S-wave velocity, and **R** is the rotation matrix around the *z* axis given by

$$\mathbf{R} \equiv \begin{bmatrix} k_x / k_r & k_y / k_r & \\ -k_y / k_r & k_x / k_r & \\ & & 1 \end{bmatrix}. \quad \text{(A5).}$$

The superscript "^{T}" indicates matrix transposition.

Using Eqs.(A.3) and (A.4), the **H** matrix in Eq.(10) becomes

$$\mathbf{H} \equiv \mathbf{U}^{+}\left(\mathbf{S}^{+}\right)^{-1} - \mathbf{U}^{-}\left(\mathbf{S}^{-}\right)^{-1} = \frac{2}{i\omega\rho c_S \cdot R} \mathbf{R}^T \begin{bmatrix} k_z^S / k_S & & \\ & k_S R / k_z^S & \\ & & k_z^P / k_S \end{bmatrix} \mathbf{R}, \quad \text{(A6)}$$

where R is the dimensionless Rayleigh function

$$R \equiv \left[1-2(k_r / k_S)^2\right]^2 + 4(k_r / k_S)^2 (k_z^P k_z^S / k_S^2) \,. \text{(A7)}$$

APPENDIX B

As an alternative to using the compliance-based equations, we can use equations based on fracture stiffness $\boldsymbol{\kappa}(x, y) = \boldsymbol{\eta}^{-1}(x, y)$. In this case, Eq.(7) in the text is replaced by

$$(\tilde{\boldsymbol{\kappa}} * [\tilde{\mathbf{u}}])(k_x, k_y) = \tilde{\boldsymbol{\sigma}}(k_x, k_y). \quad \text{(B1)}$$

$\tilde{\boldsymbol{\kappa}}$ is the Fourier transformed fracture stiffness matrix. By using the displacement discontinuity vector $[\tilde{\mathbf{u}}] = \mathbf{U}^{+}\mathbf{a}^{+} - \mathbf{U}^{-}\mathbf{a}^{-} - \mathbf{U}^{+}\mathbf{a}_{Inc}$ as the primary variable, the coefficients $\mathbf{a}^{-}$ and $\mathbf{a}^{+}$ in Eqs.(8) and (B1) are eliminated from the second equation, resulting in

$$\left(\mathbf{H}^{-1} - \tilde{\boldsymbol{\kappa}} *\right)[\tilde{\mathbf{u}}] = \mathbf{H}^{-1}[\tilde{\mathbf{u}}]_{Inc}, \quad \text{(B2)}$$

where the incident term for the displacement-discontinuity vector is defined as

$$[\tilde{\mathbf{u}}]_{Inc} \equiv -\mathbf{H}\mathbf{S}^{+}\mathbf{a}_{Inc}. \quad \text{(B3)}$$

Eq.(B3) is the displacement discontinuity vector for an open fracture (free surface). The integral equation corresponding to equation (12) is

$$[\tilde{\mathbf{u}}](k_x, k_y) = [\tilde{\mathbf{u}}]_{Inc}(k_x, k_y) + \mathbf{H}(k_x, k_y)\int_{-\infty}^{+\infty}\int_{-\infty}^{+\infty} \tilde{\boldsymbol{\kappa}}(k_x - k_x', k_y - k_y')[\tilde{\mathbf{u}}](k_x', k_y')dk_x'dk_y', \quad \text{(B4)}$$

and the Neumann series (Born series) corresponding to Eq.(14) is

$$[\tilde{\mathbf{u}}] = \left[\bar{\mathbf{I}} - i\bar{\mathbf{T}} + (-i\bar{\mathbf{T}})^2 + ...\right][\tilde{\mathbf{u}}]_{Inc} = \left(\bar{\mathbf{I}} + i\bar{\mathbf{T}}\right)^{-1}[\tilde{\mathbf{u}}]_{Inc}, \quad \text{(B5)}$$

where the operator $\bar{\mathbf{T}}$ is defined as $-i\bar{\mathbf{T}} \equiv \bar{\mathbf{H}}\bar{\tilde{\boldsymbol{\kappa}}}$. It should be noted that, in general, the fracture stiffness convolution operator $\bar{\tilde{\boldsymbol{\kappa}}}$ is not the inverse of the compliance operator $\bar{\tilde{\boldsymbol{\eta}}}$. Eq.(B4) can be written in a matrix form to be solved numerically. The resulting matrix equation is equivalent to the compliance-based equation (17) but shows faster convergence of iterative solutions at higher frequencies. This property can be used to efficiently implement the computer program to

solve for the “exact” solutions: the compliance formulation is used at low frequencies and the stiffness formulation at high frequencies.

Figure 1 Heterogeneous fractures with a variety of microstructures are modeled as a planer interface between half-spaces with spatially varying fracture compliance (springs in the figure).

Figure 2 Compliance distribution along a finite, 56 m-long fracture of the two-dimensional BEM model. Both normal and shear compliances are the same. For the three-dimensional wd-SDD model, the sinusoidal distribution extends infinitely in the *x* direction, and the identical profile extends infinitely in the *y* direction (in-and-out of the paper).

Figure 3 Comparisons between waveforms computed using the BEM and the wd-SDD method. A plane P wave is normally incident on the fractures. The first-arriving parts of the waves show very good agreement. The results of the wd-SDD method show long-lasting reverberations ("coda") due to the waves scattered long distance away from the receiver.

Figure 4 Single periodic cell for the compliance distribution of a simulated fracture. The distribution is periodic in both *x* and *y* directions. The correlation length of the distribution is 4 m (single standard deviation of a fitted Gaussian distribution), and the compliance values vary for about an order of magnitude.

Figure 5 Three-dimensional snapshots of the waves scattered by a single plane fracture at z=0, with a heterogeneous fracture compliance distribution shown in Figure 4. Both *x* and *z* direction particle displacements are shown on the surfaces of a cube cut out of an infinite medium containing the fracture. The top two rows are for a normally incident P wave propagating from the bottom of the plots, and the bottom two rows are for an obliquely incident P waves propagating from the bottom left corner of the cube.

Figure 6 *Sv*, *Sh*, and *P*-wave amplitude distributions of wavenumber components around a unit amplitude, incident *P* wave (m=n=0). Both the normal incidence case (a) and oblique incidence case (b) are shown. The frequency of the waves is 750 Hz. The color scale is saturated for components with an amplitude larger than 0.01. The line diagrams are the profiles of the

distributions cut along the line, m=0 (shown as a dotted line). The amplitudes of the wavenumber components decay quickly away from the center (incident wave).

Figure 7 Real and imaginary parts of the transmission coefficients (the most dominant specular components of P wave are compared) computed using the Born approximations of different orders up to n=5. For comparison, the 'exact' numerical solutions are also plotted. The low-frequency approximations are computed using the compliance-based Born series while the high-frequency approximations are obtained from the stiffness-based Born series.

Figure 8 Comparisons between z-direction particle motions computed by solving the matrix equation in Eq. (18) and by the 3rd-order, compliance-based Born approximation. The central frequency of the incident Ricker wavelet (P wave) is 100 Hz, and the receivers are located on both sides, 32 m away from the fracture. The results are nearly identical.

Figure 9 Magnitudes of individual terms in the Born series for a unit-amplitude, plane incident P wave. The z-direction particle displacements of transmitted P wave are shown. The n^{th}-order term of the high-frequency Born series scales as $o(1/\omega^{n+1})$. In contrast, all the terms except for the 0th order term (incident wave) in the low-frequency Born series scale as $o(\omega)$. The absolute magnitudes of the higher order terms, however, are small for this example.

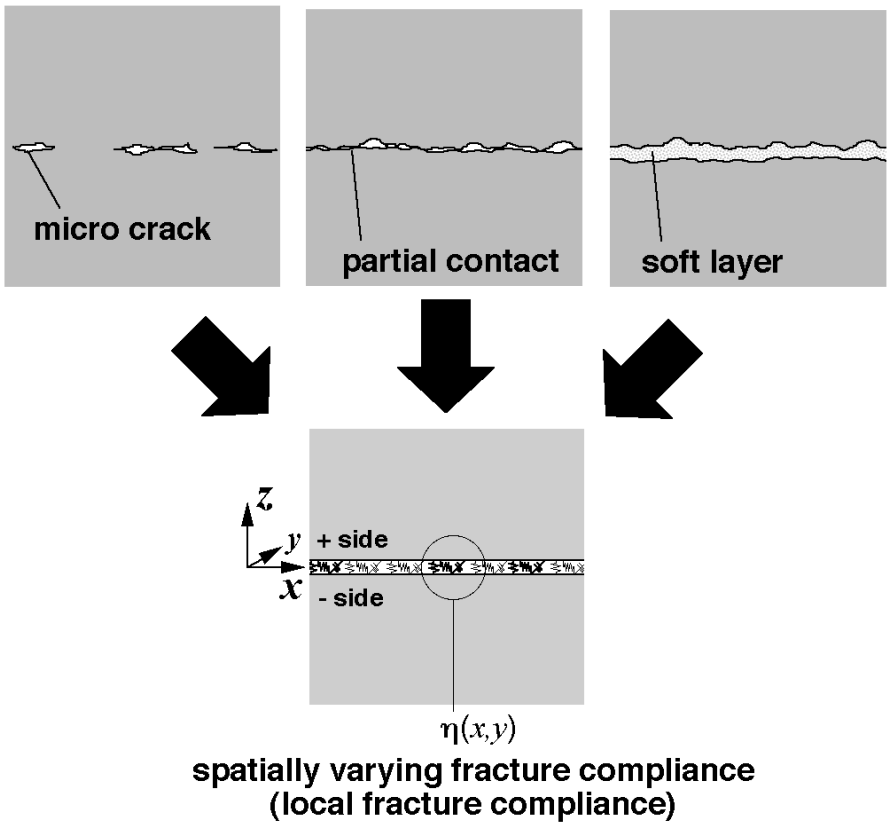
micro crack
partial contact
soft layer
z
y
x
+ side
- side
η(x,y)
spatially varying fracture compliance
(local fracture compliance)

Fig.1

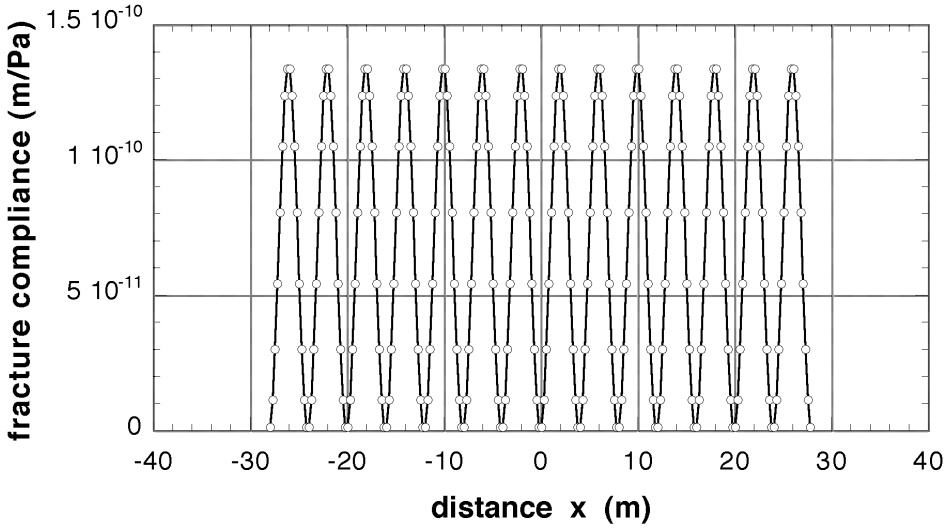
fracture compliance (m/Pa)
1.5 10-10
1 10-10
5 10-11
0
-40
-30
-20
-10
0
10
20
30
40
distance x (m)

Fig.2

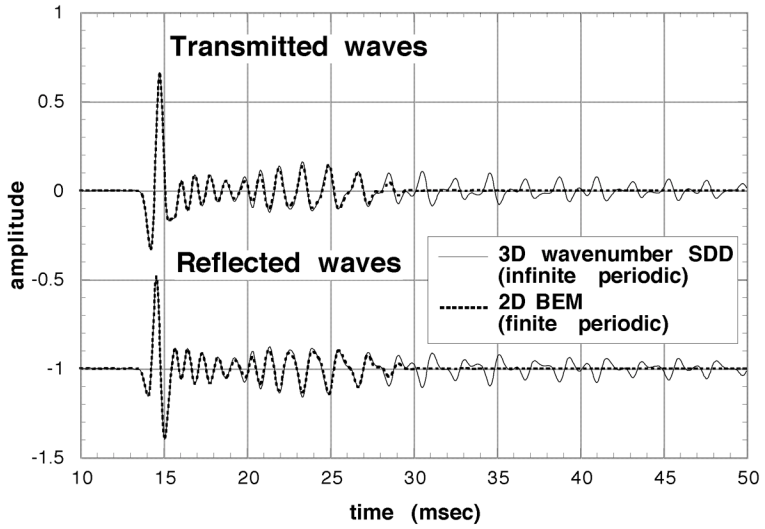
Transmitted waves
Reflected waves
3D wavenumber SDD
(infinite periodic)
2D BEM
(finite periodic)
amplitude
time (msec)
1
0.5
0
-0.5
-1
-1.5
10
15
20
25
30
35
40
45
50

Fig.3

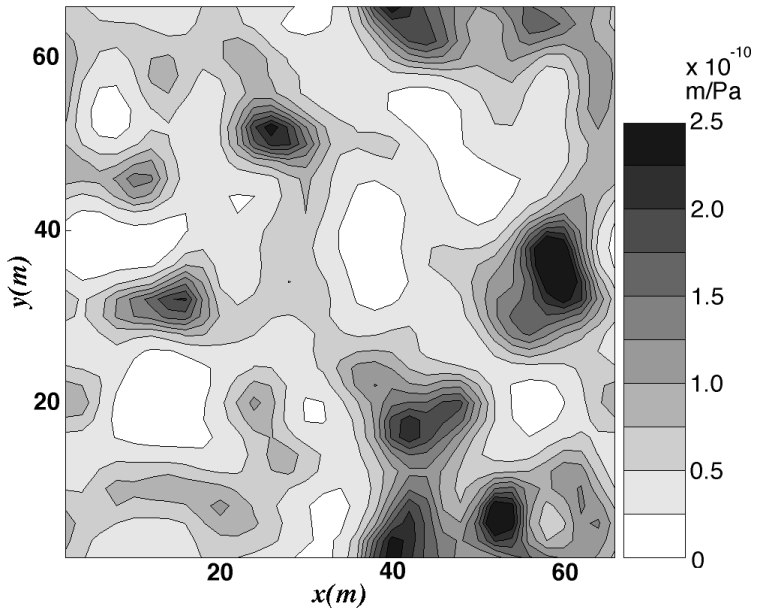
x 10^-10
m/Pa
2.5
2.0
1.5
1.0
0.5
0
y(m)
x(m)
60
40
20
20
40
60

Fig.4

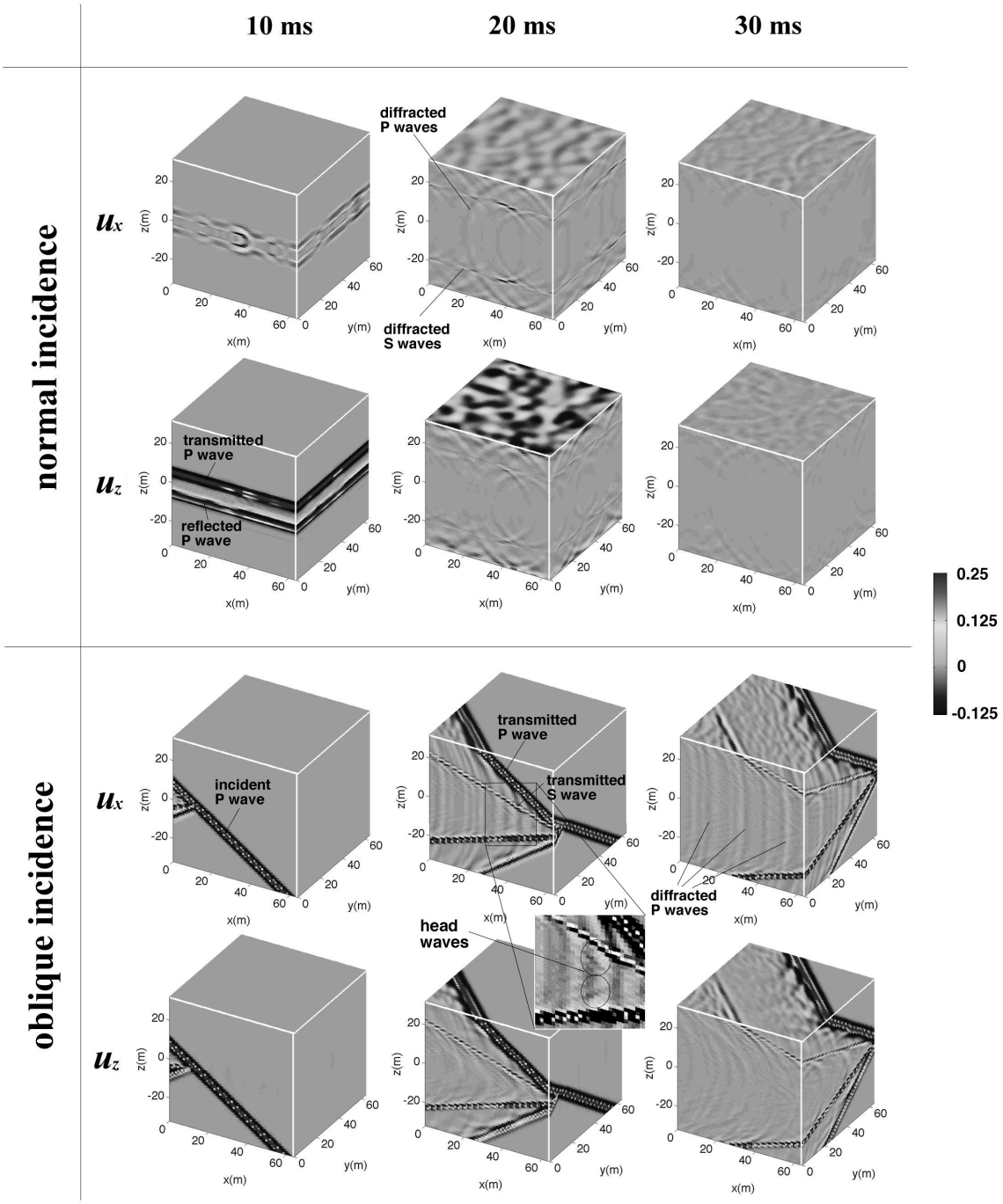
10 ms
20 ms
30 ms
normal incidence
oblique incidence
u_x
u_z
diffracted P waves
diffracted S waves
transmitted P wave
reflected P wave
incident P wave
transmitted P wave
transmitted S wave
diffracted P waves
head waves
0.25
0.125
0
-0.125
x(m)
y(m)
z(m)

Fig.5

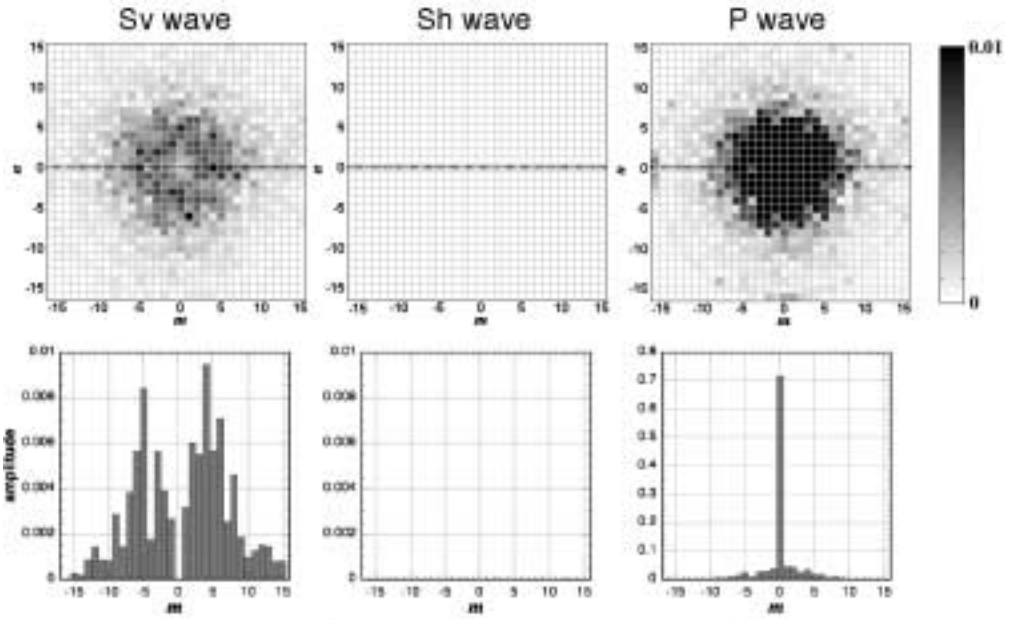

(a) Wavenumber diagrams for a normally incident P wave

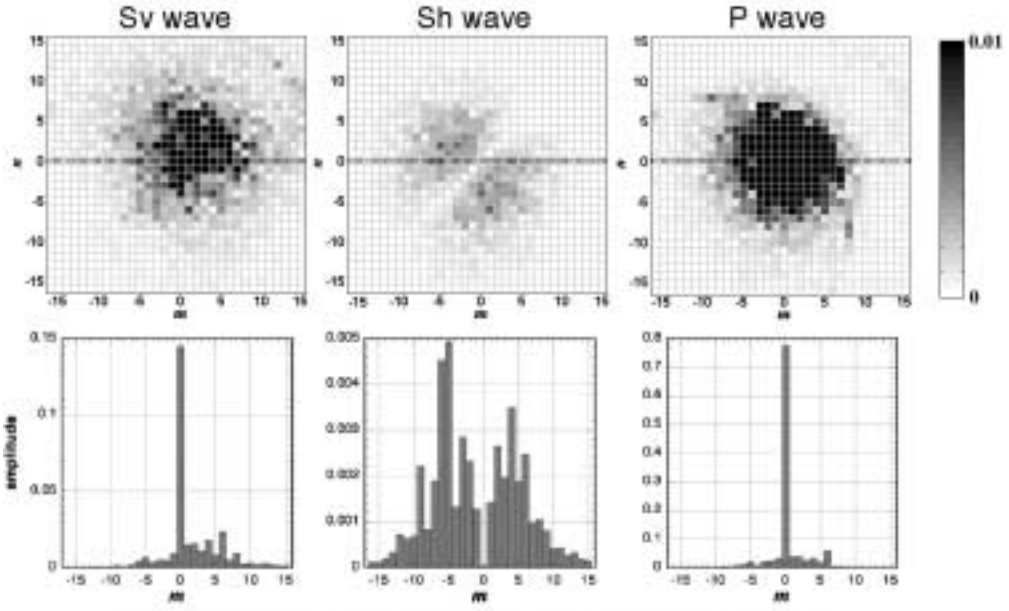

(b) Wavenumber diagrams for a obliquely incident P wave

Fig.6

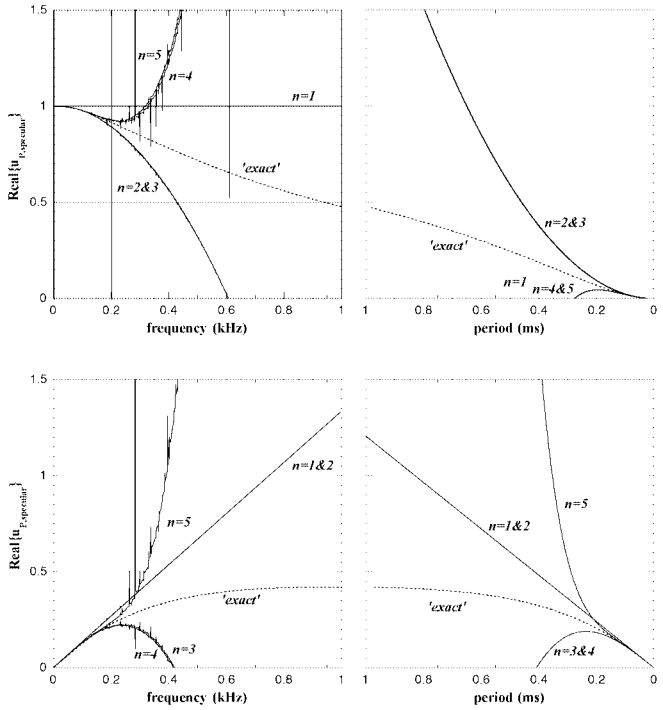
n=5
n=4
n=1
'exact'
n=2&3
frequency (kHz)
n=2&3
'exact'
n=1
n=4&5
period (ms)
n=1&2
n=5
'exact'
n=4
n=3
n=1&2
n=5
'exact'
n=3&4

Fig.7

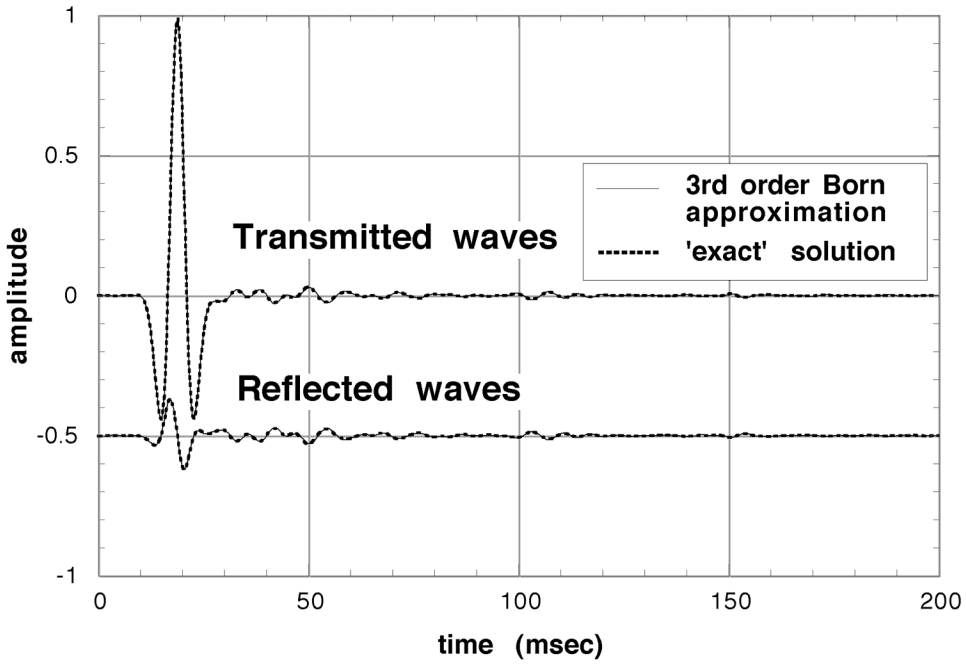
3rd order Born approximation
'exact' solution
Transmitted waves
Reflected waves
amplitude
time (msec)

Fig.8

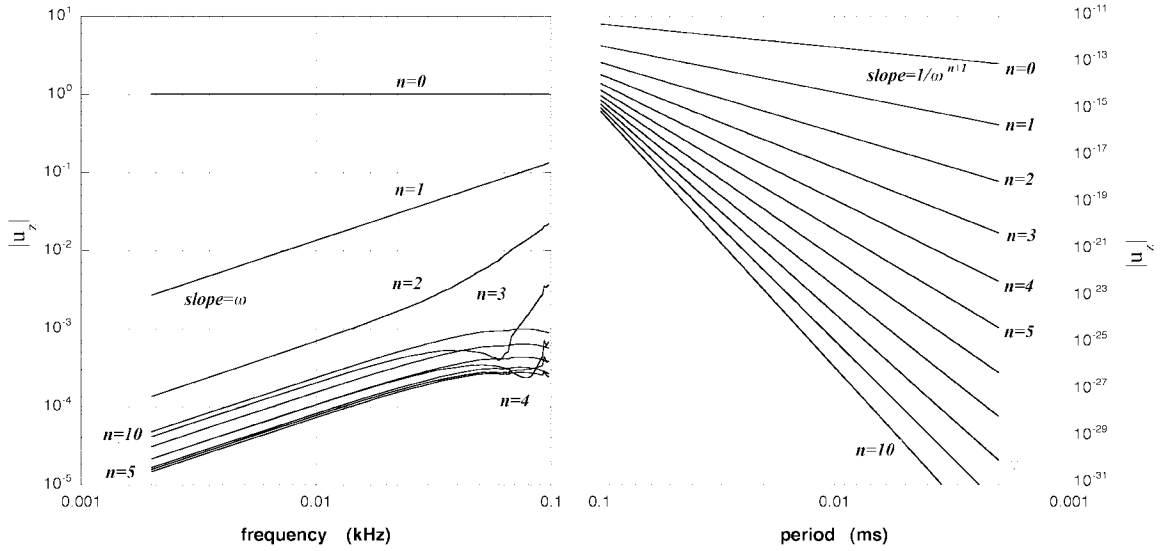
n=0
n=1
n=2
n=3
n=4
n=5
n=10
slope=ω
slope=1/ω^(n+1)
frequency (kHz)
period (ms)

Fig.9